Radiative impact of increased middle atmospheric water vapour in the aftermath of the Hunga 2022 volcanic eruption at two locations in the Northern Hemisphere

Alistair Bell[a,b], Axel Murk[a,b], and Gunter Stober[a,b]

[a]Institute of Applied Physics, University of Bern, Bern, Switzerland
[b]Oeschger Centre for Climate Change Research, University of Bern, Bern, Switzerland

Correspondence: Alistair Bell (alistair.bell@unibe.ch)

Abstract. Increases in middle atmosphere water vapour as a result of the 2022 Hunga volcanic eruption have now been detected almost globally, with above-average mixing ratios predicted to persist until around 2032. Changes in the middle atmosphere water vapour volume mixing ratio impact chemical reactions in this section of the atmosphere, can result in more favorable conditions for polar stratospheric and mesospheric cloud formation, and have a significant radiative effect on the middle atmosphere and below. For this reason, precise radiative transfer calculations are important to make accurate and precise assessments of changes to both long-wave and short-wave fluxes, and how this may impact the heating rates at different heights in the atmosphere. In this study, water vapour profiles from two microwave radiometers deployed at two different latitudes in Europe are used to analyse changes in water vapour in the aftermath of the Hunga volcano, and a line-by-line radiative transfer model is used to analyse the thermal impact of this increase over Bern, Switzerland, and Ny-Ålesund, Svalbard.

1 Introduction

The 2022 Hunga (also commonly referred to as Hunga-Tonga or Hunga Tonga-Hunga Ha'apai [HTHH]) volcanic eruption, having a volcanic explosivity index of at least VEI-5 (Terry et al., 2022) would have been a notable global event considering simply the eruptive power, with the eruption having comparable energy to the Krakatoa volcanic eruption Matoza et al. (2022). The event caused various phenomena in the atmosphere; launching atmospheric waves traveling around the Earth up through all layers including the thermosphere (Wright et al., 2022; Stober et al., 2023; Themens et al., 2022; Vadas et al., 2023b, a; Stober et al., 2024). What gave the event even more importance on a global scale, however, was the amount of water that was vapourised and then injected into the middle atmosphere, in a plume that reached above $50\,\mathrm{km}$ asl during the peak of the eruption (Millan et al., 2022) (GOES satellite images revealed that the ash plume reached 53 km (Carr et al., 2022)). It has been estimated that the mass of water vapour injected into the stratosphere during the eruption was $146\,\mathrm{Tg}$- equal to approximately $10\,\%$ of total global stratospheric water vapour, or around the same amount as enters the stratosphere from all sources globally during one year.

The water vapour in the middle atmosphere is relatively stable because of the few sinks in this part of the atmosphere. When a rare event such as the injection of water vapour into the middle atmosphere occurs, such as the case with the Hunga eruption,

this means that perturbations can have effects lasting for several years. Jucker et al. (2023) have found from climate model
simulations that the increased water vapour from the Hunga volcano is likely to last eight years or more. The climatic impact
of this has thus sparked interest in the scientific community.

Aside from the injection of water vapour into the stratosphere, a moderate amount (totalling 0.6-0.7 Tg) of sulphur dioxide
was also emitted during the entire eruption sequence (Carn et al., 2022). Whilst increased water vapour has a warming net
radiative effect at the surface due to increased long-wave absorption, sulphur dioxide, which forms sulfate aerosols in the
atmosphere, has the effect of reducing the amount of short-wave radiation that reaches the surface and, thus, results in a
negative radiative impact at the surface.

Whilst Jenkins et al. (2023) have suggested that the volcano would have a net warming effect on the global surface, meaning
that global temperature anomalies could exceed the threshold $1.5\,°C$ limit, other authors have suggested that the dominant
effect of the eruption was due to the aerosol, which would result in a surface cooling effect. Sellitto et al. (2022) estimated the
radiative effect in the weeks after the eruption to be negative at the surface $[-1.7\,\mathrm{W\,m^{-2}}]$. Schoeberl et al. (2023b) estimated
that the mean surface temperature change from the combination of a reduction in short-wave flux and an increase in long-wave
flux would be negative, with the effects causing cooling of $0.038\,°C$ for clear skies and $0.021\,°C$ for all skies (i.e. including
cloud cover) in the southern hemisphere.

Whilst providing reasonable estimates of radiative flux calculations on a global scale, and being able to investigate numerous
changes due to atmospheric composition changes, one drawback of studies using general circulation models (GCMs) is that the
radiation schemes used are heavily parameterised to keep computational resources reasonable. GCMs such as the Whole At-
mosphere Community Climate Model (WACCM) utilise correlated-k distribution methods, grouping wavelengths with similar
absorption characteristics to allow a radiative transfer scheme to represent the entire short-wave or long-wave spectrum with-
out having to calculate absorption coefficients across every absorption line. It has been postulated that such radiative transfer
schemes are accurate to within $0.20\,\mathrm{W\,m^{-2}}$ to $0.23\,\mathrm{W\,m^{-2}}$ of more accurate line-by-line calculations, and within $0.15\,\mathrm{K\,d^{-1}}$
for stratospheric heating rates (Iacono et al., 2008).

The effect of a changing radiative balance affects not only the temperature at the surface. With increased long-wave emission
or short-wave absorption, atmospheric layers may cool down or heat up in response. Around the altitude and latitude of the
maximum water vapour anomaly in the weeks following the eruption ($38\,\mathrm{hPa}$ to $10\,\mathrm{hPa}$; 30°S to 5°N), it was found that
there were correlations with negative temperature anomalies (Basha et al., 2023). Another point that appears to be of crucial
importance for the radiative balance, is how the mixing ratio of ozone responds to changes in water vapour. (Basha et al.,
2023) also found that increases in water vapour corresponded to decreases in ozone, with anomalies of up to $-0.5\,\mathrm{ppmv}$ being
collocated with increases in water vapour of around $2\,\mathrm{ppmv}$. This is explained by the production of hydroxyl radicals, which
have a net effect of reducing ozone through reactions involving hydrogen oxides. In work unrelated to the HTHH volcano, it has
also been found that cooling induced by increases in the amount of water vapour in the lowermost stratosphere has a significant
effect on the subtropical and eddy-driven jet streams which can affect weather patterns in the troposphere (Charlesworth et al.,
2023).

Several months after the eruption, a portion of the water vapour plume had been transported across the equator into the northern hemisphere, which has been proposed to have been partly due to equatorial Rossby waves generated by long-wave cooling of stratospheric air by the increased water vapour itself (Schoeberl et al., 2023a). This thermal anomaly was perhaps increased due to the separation of the water vapour, which ascended in altitude in this time period, and the aerosol layer, which descended Schoeberl et al. (2022). Already in April 2022, observations had been made of the increase in water vapour anomaly at Manu Loa at $19.5°$ N (Nedoluha et al., 2023). As of November 2023, almost all the water vapour initially injected into the middle atmosphere remained there, albeit at higher altitudes on average (Nedoluha et al., 2024), which resulted in the highest recorded mesospheric water vapour since operations began in the 1990's at Manu Loa.

Continuous observations have also been made by two radiometers designed and operated by the University of Bern. These two radiometers in Bern, Switzerland, and Ny-Ålesund, Svalbard, have continuously measured water vapour profiles in the middle atmosphere from 2006 and 2015 respectively, until today. This provides a valuable resource for estimating the increases in water vapour caused by the HTHH volcano in the three years following eruption at two locations. Two methods based on the same line-by-line radiative transfer simulator are then run to make precise calculations of the long-wave flux anomalies caused by the increase in water vapour. One of these methods is also used to calculate local heating rates from both short-wave and long-wave impacts of the water vapour changes in Bern, Switzerland.

2 Instruments

2.1 Ground-Based Radiometric Observations

Several microwave radiometers have been developed, deployed, and maintained by the University of Bern to measure atmospheric composition and temperature, particularly for the middle atmosphere (Bell et al., 2025; Fernandez et al., 2015; Sauvageat et al., 2022; Krochin et al., 2022; Shi et al., 2023). These long-term observations are ideal for investigating the impact of sudden disruptive events such as the HTHH eruption. In this study, we leverage data from two water vapour radiometers currently operated next to Bern at the mid-latitudes and at Ny-Ålesund on Svalbard covering also the high-latitudes (Schranz et al., 2020).

2.1.1 MIAWARA

The MIddle Atmosphere WAter vapour RAdiometer (MIAWARA) is a 22 GHz radiometer designed for long-term monitoring of water vapour in the middle atmosphere. It has been operated by the Institute of Applied Physics (IAP) at the University of Bern since April 2002 and was installed at the Zimmerwald Observatory near Bern, Switzerland, in 2006.

The observational frequency is centred on the 22.235 GHz water vapour absorption line. A balancing calibration scheme using a reference view that optimizes noise and linearity (Forkman et al., 2003). Hot and cold targets are used, with the sky at a high elevation angle serving as the cold target. Currently, two spectrometers are used. One FFT spectrometer: the Aquiris

AC-240 with 61 kHz channel spacing and a Software-defined radio (SDR) USRP X310 with two input receivers, and 12.2 kHz channel spacing, and a 14-bit ADC for reduced bias and improved linearity.

90 The retrieval of water vapour profiles is handled by the ARTS (atmospheric radiative transfer software) Buehler et al. (2018), with an optimal estimation algorithm, utilising the Levenburg-Marquart algorithm for iterative updates, and a priori profiles taken from ECMWF analysis climatology and MLS water vapour climatology. The time series from 2011 has been recently reprocessed, from which this analysis has been conducted (Bell et al., 2025).

2.1.2 MIAWARA-C

95 The MIddle Atmospheric WAter vapour RAdiometer for Campaigns (MIAWARA-C) was based on the original design of the MIAWARA, but specifically designed for measurement campaigns (Tschanz et al., 2013) (data access at: Bell (2025)). Developed by the University of Bern, MIAWARA-C is more compact and can be operated remotely. The observational frequency is also centred on the 22.235 GHz absorption line, and makes use of the balancing calibration routine. In addition, the radiometer was upgraded to include a dual-polarization receiver. This allows the instrument to utilise independent measurements from two
100 receiver channels corresponding to the same air mass, which are used together to reduce the measurement noise. After several campaigns, including Bern (47°N, 7°E) and Sodankylä (67°N, 27°E) from 2010 to 2013, the radiometer was moved to the AWIPEV research base in Ny-Ålesund, Svalbard (79°N, 12°E) where it has been based since September 2015 (Schranz et al., 2018, 2019; Shi et al., 2024).

The retrieval process is similar to that explained in Bell et al. (2025), but has one key difference in that a priori water vapour
105 profiles for the lower stratosphere contain information from the ECMWF forecasts corresponding to the retrieval time.

2.2 Space-Borne

Space-borne instruments can be an immensely useful resource for tracking and monitoring water vapour in the middle atmosphere: the key advantage that is offered when compared to ground-based instrumentation is the horizontal coverage of measurements. Depending on orbit geometry and instrument field of view the entire globe can be observed. However, the
110 revisit time for specific geographic locations is much lower when contrasted to ground-based sensors.

2.2.1 Aura-MLS

The Microwave Limb Sounder (MLS) aboard the Aura satellite is a microwave radiometer with five independent receivers that provide high-resolution spectral data. It retrieves at least 15 atmospheric constituents (including water vapour) and temperature profiles at heights from $5\,\mathrm{km}$ to $80\,\mathrm{km}$ (Waters et al., 2006; Schwartz et al., 2008). MLS is often used as a reference for other
115 middle atmosphere measurements due to its frequent and co-located measurements covering all latitudes from 82° S to 82° N. It has also been an invaluable resource for tracing the water vapour plume evolution in the aftermath of the Hunga eruption (attached video material documenting the global spread from MLS).

The MLS science team has implemented a "duty cycle" for the 190-GHz observations, which include H_2O, N_2O, HCN, and upper stratospheric HNO_3, to conserve the remaining life of the instrument. This involves reactivating the subsystem for
120 approximately six days each month, with possible adjustments based on the aging of the receiver (NASA JPL, 2024). The instrument is also not expected to make further observations beyond Spring 2026 at the latest due to its de-orbiting. However, technical issues can even shorten the remaining lifetime substantially.

2.2.2 ACE-FTS

The ACE-FTS (Atmospheric Chemistry Experiment Fourier Transform Spectrometer) aboard the SCISAT-1 satellite uses high-
125 resolution solar occultation to infer atmospheric constituents, including water vapour, and measures vertical profiles from the cloud tops up to 150 km. The instrument performs two soundings per orbit, during sunrise and sunset, which means that the temporal coverage provided by the satellite is much reduced compared to Aura-MLS, and revisit times are variable. For water vapour, the retrieval height is limited to $101\,\mathrm{km}$. The quality of the v2.2 H_2O dataset assessed by Sheese et al. (2017) indicated a consistent positive bias in the measurements from the lower stratosphere up into the mesosphere, typically around 3% to 8%
130 compared to other datasets.

3 Water Vapour Evolution

Much has been written about the evolution of the initial water vapour plume (Schoeberl et al., 2023a; Nedoluha et al., 2024). To summarise this: shortly after the eruption, the water vapour plume was initially confined mostly to the Southern Hemisphere. Within a month, there was a significant northward movement of the plume across the equator, which was attributed to infrared
135 cooling effects associated with the high levels of water vapour, which likely induced equatorial Rossby waves. These waves helped to push the water vapour across the equatorial barrier into the Northern Hemisphere. During the descending phase of the Quasi Biennial Oscillation (QBO), there was also a notable cross-equatorial transport of water vapour, which occurred along-side changes in the Brewer-Dobson circulation. The shift in the QBO and associated circulation dynamics further transported water vapour across the equator, extending its impact and distribution. Almost all of the water vapour that was initially injected
140 into the stratosphere remained above the tropopause two years after the eruption.

With MLS data, the transport of the water vapour anomaly is visible to as far north as $80°$. This should affect the water vapour profiles above the observation sites in Bern, Switzerland and Ny-Ålesund, Svalbard. An animated graphic has been produced showing the meridional, and vertical transport of water vapour around the globe (see Supplementary Material).

A comparison of the observations from MIAWARA and MIAWARA-C to MLS and ACE-FTS was performed to verify
145 the retrievals, shown in figure 1; whilst MIAWARA over-estimates and the ACE-FTS underestimates relative to Aura-MLS at 1hPa, the pattern of observations remains constant and all show significant increases in water vapour anomalies from mid-2022. Water vapour measurements above Ny-Ålesund exhibit for the MIAWARA-C and ACE-FTS slightly lower values compared to MLS retrievals, but again resemble the overall seasonal morphology with reasonable agreement. This aligns with other cross-comparisons with these instruments and reanalysis data performed before (Shi et al., 2023). It can be noted that for this
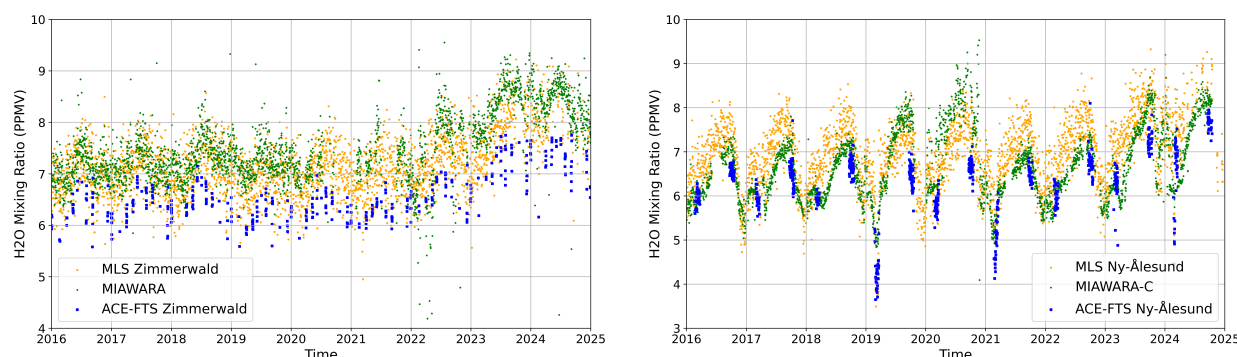
Figure 1. Water vapour at 1hPa retrieved from the MIAWRARA, MLS and ACE-FTS instruments between 2018 and March 2024.

comparison, all ACE-FTS measurements were taken from within 5 °latitude and 25 °longitude of the observation sites (either Zimmerwald, BE, Switzerland, or Ny-Ålesund, Svalbard). Due to the nature of the orbit and observation method, which allows measurements only at sunset and sunrise at fixed local time, the ACE-FTS has relatively few water vapour profiles, and these are clustered close to the beginning and end of the year for Ny-Ålesund, which is located at a very high latitude (78.9° N).

The observations from Zimmerwald, BE, show that already in summer of 2022, water vapour mixing ratios at $0.1\,hPa$ are above preceding years by around 0.5-1 ppmv between day 200 and day 300 of the year (mid July until late October). In 2023, however, unprecedentedly high water vapour mixing ratios were recorded at this pressure level, with almost $9\,ppmv$ being recorded on September 5th 2023 compared to 6.5 - 7.0 ppmv as had been recorded on this date throughout all years between 2015 and 2021.

In Ny-Ålesund, whilst above average water vapour mixing ratios were also present, this is only from summer 2023. It is worth here noting that the observations from MIAWARA-C during 2020 are in some disagreement with the observations from the ACE-FTS and MLS (MIAWARA-C has a positive bias compared to both instruments in this year, compared to previous years where there is a negative bias vs MLS and no bias compared to ACE-FTS). An anomaly similar to that recorded by the MIAWARA-C throughout 2020 then persisted throughout 2024 at 0.1 hPa and 1 hPa, before reducing to near similar levels at the end of 2024.

4 Flux Analysis

4.1 Longwave down-welling Fluxes

Water vapour strongly influences the Earth's energy budget because it is an effective absorber and emitter of infra-red radiation within specific frequency bands. In the troposphere, water vapor is the most abundant greenhouse gas, and fluctuations in its concentration strongly modulate surface temperatures by altering the radiative fluxes traveling both upwards (outgoing longwave radiation) and downwards (radiation from the atmosphere to the surface). However, the tropospheric lifetime of water vapor is limited by condensation and precipitation processes. As a result, even substantial injections of water vapor into
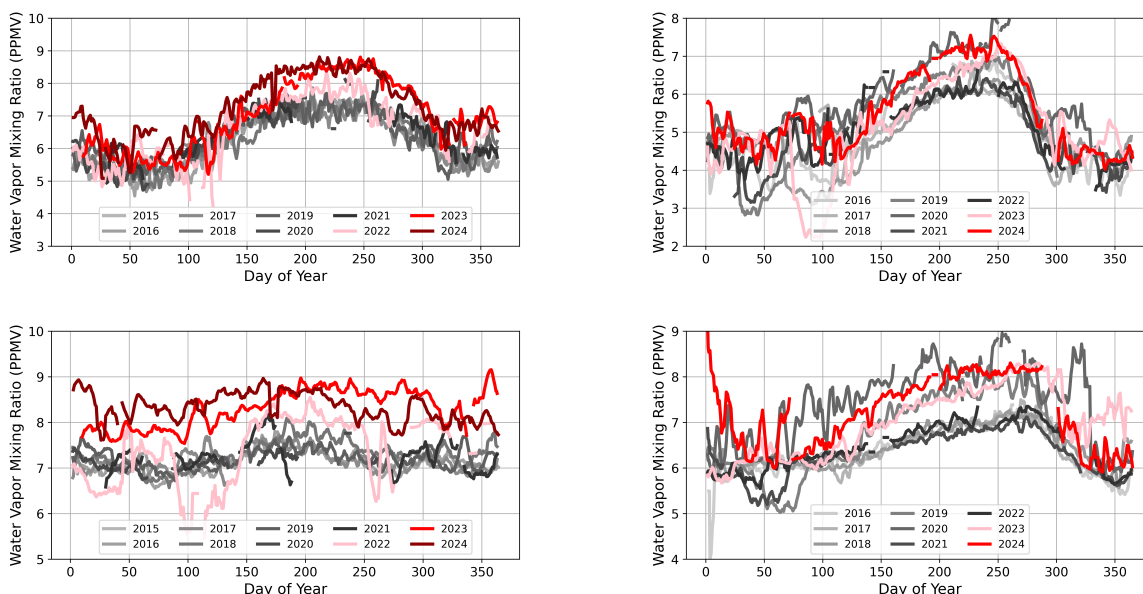
Figure 2. Water vapour with day of year, for years between 2015 and 2024 (for MIAWARA; left) and 2018 and 2024 (MIAWARA-C; right) at 0.1 hPa (top row) and 1hPa (bottom row).

the troposphere—such as the one caused by the Hunga volcano eruption—will not persist for long and therefore will have only short-lived effects on tropospheric radiative fluxes.

In contrast, injections of water vapor into the middle atmosphere (the stratosphere and lower mesosphere) can remain there

175 for much longer, on the order of years to decades, because condensation and precipitation are far less effective at those altitudes. As previously discussed, the Hunga volcano's injection of water vapor into the middle atmosphere could therefore influence the climate for about a decade. This is consistent with findings from Solomon et al. (2010), who demonstrated that a reduction in stratospheric water vapor contributed to slower surface warming (by approximately SI25 %) between 2000 and 2009, implying that any increase in stratospheric water vapor would likely accelerate warming over similar time spans.

180 It is orthodox in flux calculations for climate studies to calculate changes to downward fluxes at the surface (with the obvious application of surface heating rates). We show below, however, downward flux calculations made at the top of the troposphere, and at the lower measurement response limit of the microwave radiometer observations at 10 hPa. As flux calculations are shown only for single points (as opposed to zonal means or for the entire globe), interannual variability of weather conditions in the troposphere will affect the flux values to a large extent, and the signal coming from the middle atmosphere can be harder

185 to disentangle from greater or lesser cloud cover, for example. Furthermore, it may be argued that since most down-welling radiation in the thermal infrared wavelengths is absorbed by the troposphere and the surface, affecting the overall heat dynamics and atmospheric stability, the longwave fluxes at the top of the troposphere could be more pivotal in determining global climate patterns than those at the surface.

Monitoring the top-of-atmosphere energy balance is also important for understanding the overall sign and magnitude of
190   impacts of atmospheric composition change on the net warming or cooling effect on the climate system, as it captures the
energy flow for the whole Earth system, in contrast to downwelling surface flux measurements, which focus on the local signal
at the surface. A brief analysis of the top-of-atmosphere upward longwave flux is thus included in the analysis.

4.2   Methods

Radiative transfer simulations are essential for accurately estimating fluxes and heating rates in the atmosphere, but such calcu-
195   lations often become computationally intensive when carried out at very high spectral resolution or across many atmospheric
profiles. To address this challenge, we compare two approaches— through simulated annealing and lookup tables—which
aim to reduce the computational load without significantly compromising accuracy. By optimising the selection of frequency
points (simulated annealing) and reusing pre-computed absorption coefficients (lookup tables), repeated simulations can be
performed more efficiently for the specific case of examining the impact of composition change on radiative effects.

4.2.1   Simulated Annealing Method

In this study, a simulated annealing method is employed to optimise frequency vectors for radiative transfer simulations,
adapting methodologies described by Buehler et al. (2010) and Kirkpatrick et al. (1983). This is initiated with a predefined set
of frequencies that are evenly spaced, from which a series of adjustments of the frequency vector is made to minimise a cost
function Λ, which evaluates the deviation between simulated irradiance outputs from a high-resolution reference dataset. The
205   cost function is defined in equation 1, as a function of the integrated value of the absolute value of the difference between the
high-resolution and low-resolution spectra, plus the absolute difference in the integrated spectral intensity between the high-
resolution and low-resolution spectra. In this equation, $\mathbf{I}$ is a cubic spline interpolation function (SciPy Community, 2024). The
cost function was chosen to take into account both the difference in spectral irradiance at each frequency, and the difference in
between the integrated value of this to balance the fact that the spectral distribution of irradiances will change with different
210   atmospheric profiles and angles which the radiative transfer is calculated at, but also to take into account the fact that the
low-resolution interpolated values would always be negatively biased compared to the high-resolution reference simulation if
the integrated spectra were not considered. The factor of two applied to the first term was found empirically to optimise the
balance between the two terms.

$$\Lambda = 2 \cdot \int_{f_{\min}}^{f_{\max}} |\text{Intensity\_HR}(f) - \text{I}(\text{Intensity\_LR}, f_{\text{LR}}, f)| \, df + \left| \int_{f_{\min}}^{f_{\max}} \text{Intensity\_HR}(f) \, df - \int_{f_{\min}}^{f_{\max}} \text{Intensity\_LR}(f) \, df \right| \tag{1}$$

215   The process begins by randomly selecting an initial frequency vector and calculating its cost value by comparing the irradi-
ance values provided by the interpolation against the reference spectra. During each iteration of the annealing process, a new
candidate set of frequencies is generated by slightly modifying the current set. The new set comprises the old set, with a single
frequency replaced by another. The replacement frequency is either one of the 30 frequencies with the maximum difference
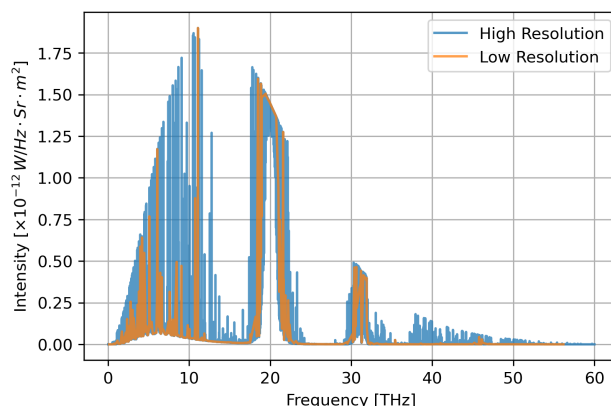
Figure 3. Spectral Intensity of the high-resolution- containing 4000 evenly spaced frequency points- and the low resolution- containing 400 frequency points- spectra at a hight of 30km and a zenith angle of $30°$

.

when the interpolated set compared to the reference set, or a random frequency in the set of reference frequencies that is not

220 currently used (a $50\,\%$ probability is used to decide which, on each iteration). This new set is evaluated, and if it shows improved or equivalent performance- guided by a probabilistic acceptance based on the simulated annealing temperature- it is accepted as the new solution. The temperature parameter decreases with each iteration, reducing the probability of accepting sub-optimal solutions as the process progresses, thereby refining the selection towards a globally optimised set of frequencies.

The frequencies used for the radiative transfer analysis are depicted in Figure 3. While the low-resolution simulation lacks

225 many of the finer spectral features, the integrated intensity between the high- and low-resolution spectra shows no significant difference at 18 km asl. This indicates that the selected frequency vector adequately represents the spectrum in question.

The goal of this optimisation is to enhance the computational efficiency and accuracy of radiative transfer simulations. This approach uses the ARTS radiative transfer simulator to simulate outputs at 19 angles between the zenith and the horizon. Pencil beam calculations are made for the 400 frequencies previously selected for their representation of the total flux. The total flux

230 is then found by integrating over all frequencies and 15 elevation angles between $0°$ (zenith) and $90°$ (horizon).

4.2.2 Lookup Table Method

Radiative transfer calculations typically involve determining the absorption coefficients for each absorbing species, across various pressure levels, and for each atmospheric path. This process can be computationally intensive and time-consuming, especially when performed repeatedly across many atmospheric profiles. To streamline these calculations, one effective approach

235 is to use a lookup table. Instead of recalculating the absorption coefficients for every new simulation, a lookup table is created and populated with data calculated at specific frequencies beforehand. This table includes pre-computed values for different conditions and parameters relevant to radiative transfer, such as gas concentrations, pressure levels, and temperatures.

Once established, this lookup table can be quickly referenced in subsequent model runs. By doing so, the model bypasses the need to perform detailed absorption coefficient calculations from scratch each time, thus substantially reducing the computational load. This approach can lead to significant savings in computational time, particularly if the frequency vector remains unchanged across all simulations. A python wrapper to perform fast flux calculations to work with ARTS has recently been developed (pya, 2024), which allows the set-up of flux calculations using the efficient lookup table method. It also takes advantage of recent developments to ARTS, which has expanded the frequency range of possible radiative transfer simulations from microwave and infra-red bands to also include visible and ultra-violet bands (Brath et al., 2024).

4.3 Method Comparison

To verify the radiative transfer calculations, long-wave down-welling fluxes are simulated from a recent climatology (2016 - 2021) of water vapour profiles retrieved with the MIAWARA radiometer. The same is done with the water vapour profiles retrieved between 2022 and 2024 with the daily water vapour profiles retrieved from the instrument. By performing simulations with both the lookup table and the full ARTS method, the calculated fluxes can be compared, and an error estimate of the model assumptions can be made.

As may be seen from figure 4, there is a small difference between the absolute values of fluxes that are calculated by the two methods. Although the lookup table method calculates stronger (more negative) fluxes between winter and mid-summer, stronger fluxes are calculated by the full ARTS method in the late summer and Autumn, coinciding with the largest water vapour anomalies observed throughout the period shown. The mean difference between the two methods is $0.075\,\mathrm{W\,m^{-2}}$, with the lookup table method calculating stronger fluxes, and the standard deviation of $0.077\,\mathrm{W\,m^{-2}}$, or $0.4\,\%$.

Despite this, the anomalies predicted by both methods, by comparing fluxes simulated from the climatology to fluxes calculated in the post-eruption period, a very good agreement is found. Throughout the period, the entire ARTS method showed more intense fluxes by a mean of $0.0017\,\mathrm{W\,m^{-2}}$, with the standard deviation of the differences being $0.003\,\mathrm{W\,m^{-2}}$ or $0.2\,\%$

The simulated annealing method produces an increase in the down-welling flux by $0.016\,\mathrm{W\,m^{-2}}$ between January 2016 and March 2024, whilst the lookup table method calculates an increase by $0.014\,\mathrm{W\,m^{-2}}$, corresponding to a $0.1\,\%$ increase in total down-welling flux at this height. Due to the faster computation time, the lookup table method was used for further calculations presented.

4.4 Shortwave Radiative Impact

As highlighted in section 1, short-wave fluxes need to also be considered when making assessments of total radiative effects of changes in atmospheric composition, i.e. how radiation coming from the sun is attenuated and induces atmospheric heating. Previous studies analysing shortwave flux effects from Hunga-induced atmospheric composition changes have focused on the impact of increased aerosol concentrations on solar fluxes; either being absorbed or scattered, having the result that short-wave fluxes at the surface were reduced in the period following the Hunga eruption (Sicard et al., 2025). Another impact is caused directly by the increase in water vapour: water vapour molecules scatter and absorb light in the short-wave part of the spectrum, allowing changes in the concentration of this gas to impact the down-welling fluxes and induce local heating effects.
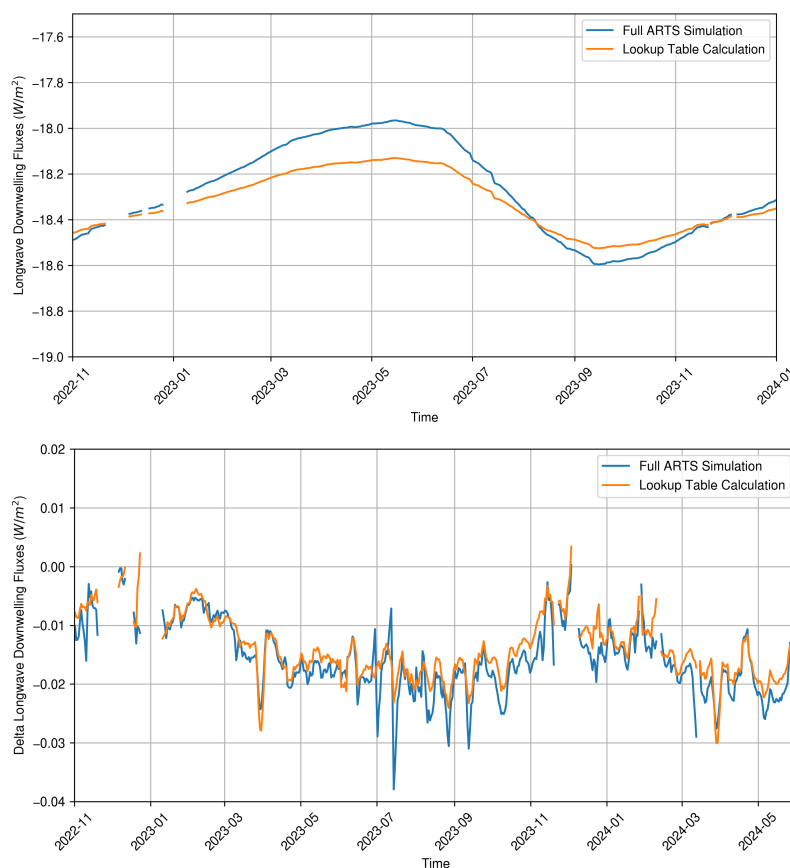
Figure 4. The long-wave down-welling flux anomaly above Zimmerwald, Bern, at 14 km, simulated from atmospheric profiles using the full radiative transfer code, and the lookup table method. The negative sign corresponds to a positive flux in a downwards direction, hence a negative anomaly represents a stronger downward flux.

The propagation of solar fluxes is a function of the zenith angle of the sun relative to the observer's position, and thus are a function of the time of day, but also highly seasonal dependent at high (arctic) and low antarctic latitudes.

A computation of change in the mean down-welling short wave fluxes was also calculated using the lookup table method. To calculate the impact that the changes in water vapour had on fluxes at the tropopause, the radiative transfer code is run at wavelengths of $300\,\text{nm}$ to $5000\,\text{nm}(60\,\text{THz}$ to $1000\,\text{THz})$ at a wavelength resolution of $2.35\,\text{nm}$. The included species are H_2O, O_2, CO_2, CO_4, and O_3. The solar flux entering at the top of the atmosphere is calculated for a fixed earth-sun distance of $1.495\,978\,707 \times 10^9\,\text{km}$, and the solar spectrum set as that recorded in May 2004 Coddington et al. (2017). Both absorption and scattering of atmospheric species are considered, but not emission.

The relative position of the sun to the surface is calculated using the PyEphem python library (Rhodes, 2023). From this package, the right ascension and declination of the sun are found from a precise date and time, from which the solar zenith

11

longitude and latitude (the Earth's longitude and latitude at which the sun is directly overhead) are calculated. These serve as inputs to the lookup table flux calculation package, and so combined with an atmospheric profile allow the calculation of down-welling short-wave fluxes.

As with the long-wave calculations, a standard atmospheric profile of all other atmospheric constituents is used, with a climatological temperature profile, and only the water vapour profile taken from measurements. For the climatological flux calculation, the average water vapour data from 2016 to 2021, based on the day of the year, is used. To accurately compare solar fluxes, the sun's position must match exactly. Therefore, in this study, the climatology was calculated based on the sun's position during the post-Hunga eruption period, specifically between 2022 and 2024. To estimate the daily mean solar down-welling flux, calculations were performed for each hour when the solar zenith angle was less than 95 degrees (i.e. when the sun was above the horizon, or less than $5°$ below the horizon). Then these results were interpolated to the minute resolution using a cubic spline method (SciPy Community, 2024). Finally, the daily mean down-welling flux was calculated as the average of these interpolated values.

4.5 Flux Analysis from Zimmerwald and Ny-Ålesund

One key difference in the retrieval technique between the measurements from Zimmerwald and Ny-Ålesund is that whilst those from Zimmerwald have a static a priori water vapour profile (taken from a climatological profile which has its source from ECMWF IFS analysis and MLS observations), the retrievals from Ny-Ålesund takes the lower a priori profile from the ECMWF analysis valid closest to the MIAWARA-C observation time. This means that below the lower measurement response limit of the MIAWARA (typically around 30 km or 10 hPa), water vapour profiles may deviate from the climatology even if there is a significant error in the a priori profile. For this reason, downwelling fluxes were calculated again at 10 hPa at Zimmerwald and Ny-Ålesund.

The anomalies presented in figure 5 show a positive response (meaning less downwelling flux) for solar flux and a negative response for infrared fluxes for almost all the period analysed after 2023 for both locations. The reduction in shortwave flux has a seasonal dependence due to the difference in the top of atmosphere downwelling solar flux throughout the year, as well as the observations, presented having the general characteristic of a greater water vapour mixing ratio anomaly in summer compared to winter. The seasonal cycle is even more profound in Ny-Ålesund (at $79°$ North) compared to Zimmerwald (at $47°$ North), where the polar night lasts for four months.

The mean downwelling anomaly at this pressure level in Zimmerwald was $0.20\,\mathrm{W\,m^{-2}}$ ($0.22\,\mathrm{W\,m^{-2}}$ from longwave only) for 2023 and $0.19\,\mathrm{W\,m^{-2}}$ ($0.21\,\mathrm{W\,m^{-2}}$ from longwave only) for 2024. Above Ny-Ålesund, this was $0.16\,\mathrm{W\,m^{-2}}$ ($0.17\,\mathrm{W\,m^{-2}}$ from longwave only) for 2023 and $0.23\,\mathrm{W\,m^{-2}}$ ($0.24\,\mathrm{W\,m^{-2}}$ from longwave only). This demonstrates therefore a slight increase in the total downward radiative fluxes coming from the mid-stratosphere during 2023 and 2024 at both locations as a result of the Hunga-induced water vapour increase.

For completeness, the top of atmosphere upwards fluxes are also analysed. In contrast to the downward flux measurements, part of the atmosphere cannot be simply excluded from these measurements to avoid the previously discussed impact of the measurement a priori profile on the upward fluxes. As is shown in Figure 6, the impact of the water vapour increase on the top
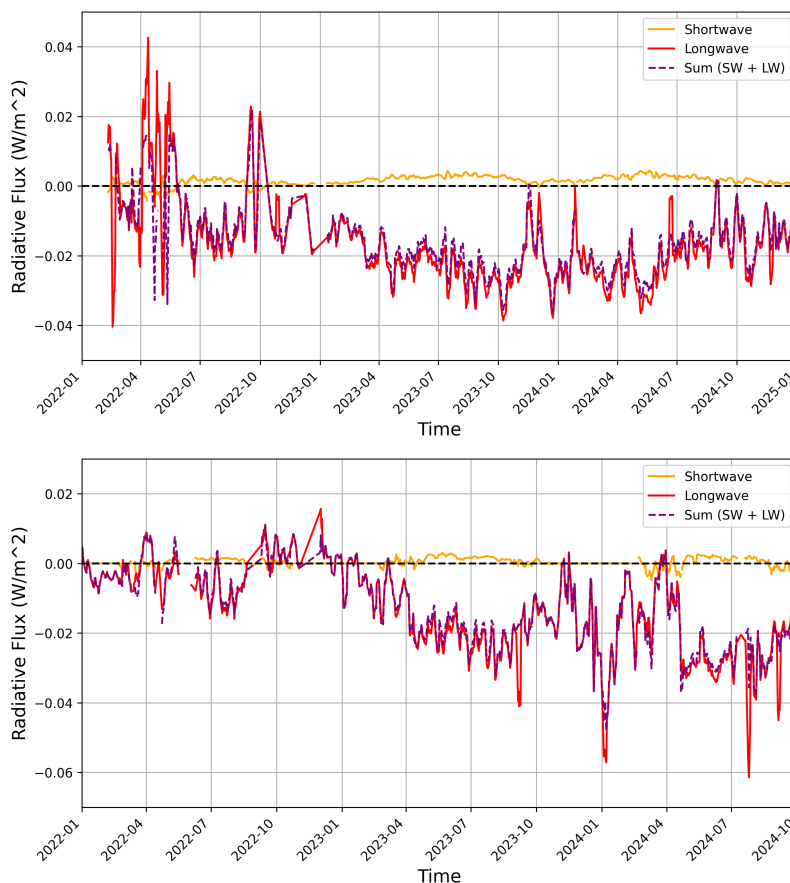
Figure 5. The short-wave and long-wave down-welling fluxes at 10hPa above the site of Zimmerwald (top) and Ny-Ålesund (bottom).

of atmosphere upward fluxes is positive at Zimmerwald, indicating a cooling effect on the climate as a whole, and negative at Ny-Ålesund. The reason for the increase in up-welling long-wave flux is here likely due to the altitude of the maximum water vapour anomaly- i.e. in the upper stratosphere and lower mesosphere. As the thermal gradient is positive in the stratosphere, the additional water vapour at those higher altitudes is effectively radiating more thermal energy out to space, thus increasing the outgoing long-wave flux. By contrast, at Ny-Ålesund, the bulk of the water vapour increase extends to lower altitudes (and cooler stratospheric conditions), thereby inhibiting the net emission of energy to space. As a result, the top-of-atmosphere flux anomaly becomes negative there, implying less energy is lost to space and thus a potential warming effect.

4.6 Local Heating Rate Anomaly

Whilst the increasing opacity caused by increases in water vapour results in long-wave emission, the local effect is one of cooling, assuming that all other effects remain constant. The lookup table method, described above and used to calculate
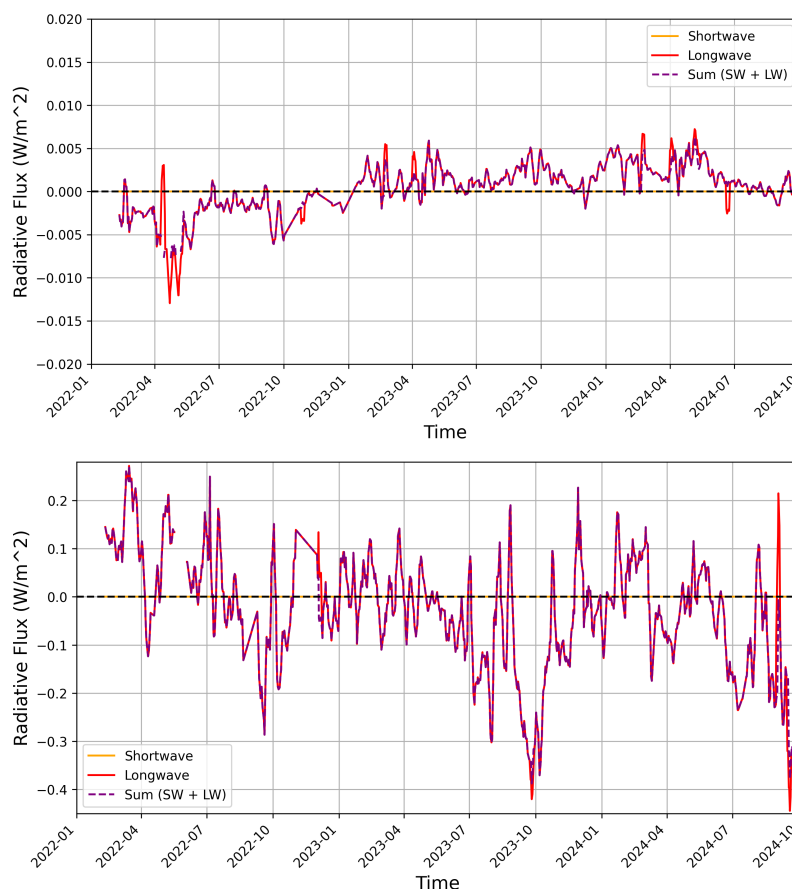
Figure 6. The short-wave and long-wave up-welling upwelling fluxes at the top of the atmosphere above the site of Zimmerwald (top) and Ny-Ålesund (bottom).

325 down-welling long-wave fluxes, was also used here to calculate the heating rates in the atmosphere, using the climatology that formed the basis previously, as well as with atmospheric profiles using the measured water vapour profiles as performed above.

The mesosphere exhibits an atmospheric circulation from the summer pole to the winter pole, as air rises from the summer pole, and is transported horizontally at mesospheric altitudes and descends over the winter pole, which is often referred to as residual circulation (Lindzen, 1981; Smith, 2012; Becker, 2012). Temperature anomalies can affect this flow by affecting

330 temperature gradients. However, temperatures are also affected directly by the strength of the circulation due to the vertical and horizontal potential temperature gradients in the middle atmosphere. In Yu et al. (2023), results are presented showing that in August 2022, southern hemispheric mesosphere cooling rates due to increased long-wave radiation and due to changes in dynamics were of the same amplitude.

The heating rate profile throughout 2023 and 2024 reveals that during these years, there was increased water vapour-induced

335 radiative cooling compared to the 2016-2022 climatology at pressures below $10\,\text{hPa}$ on average for both Zimmerwald and
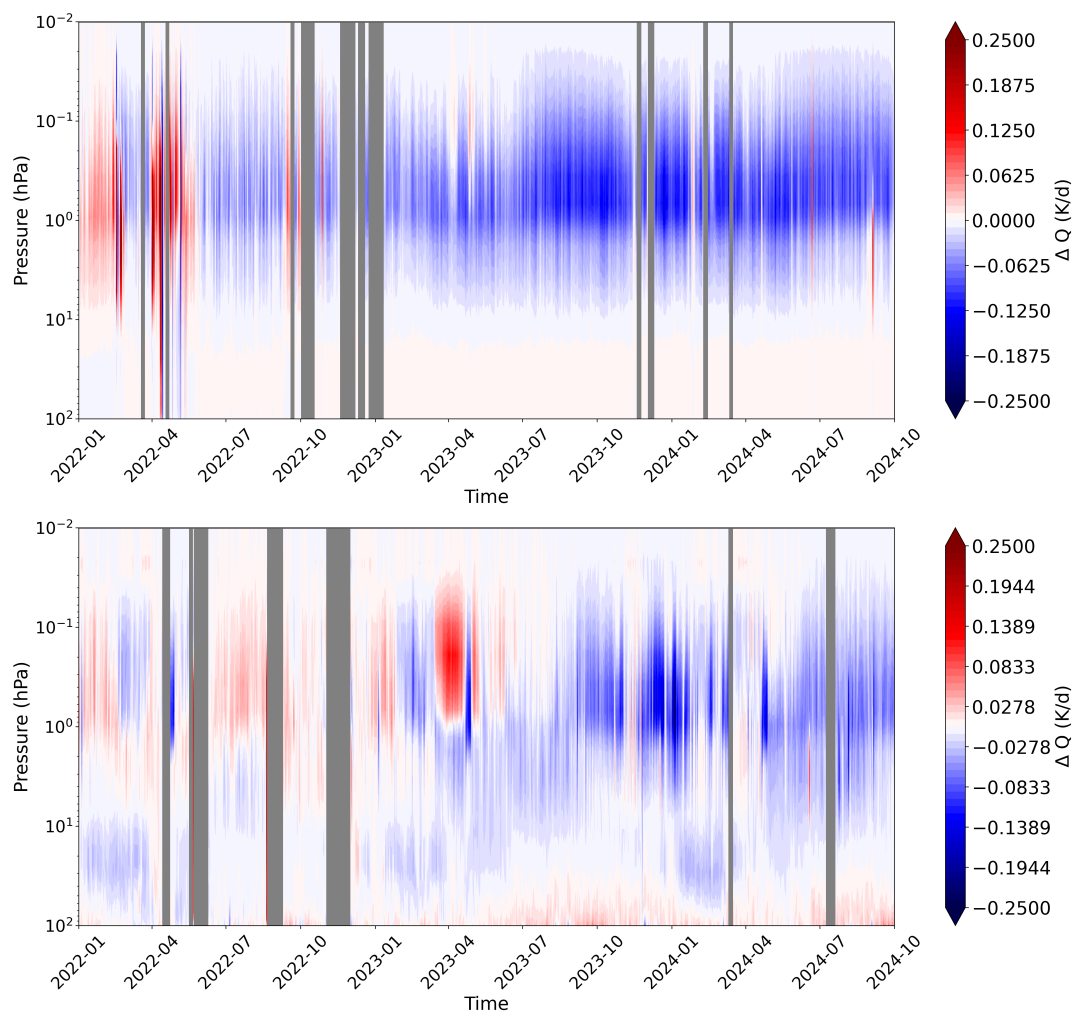
Figure 7. Heating rate anomaly profiles from long wave emission and absorption, calculated above Bern, Switzerland (top) and Ny-Ålesund, Svalbard (bottom) between 2022 and 2024.

Ny-Ålesund. At Zimmerwald, the heating rate anomaly at $0.8\,\mathrm{hPa}$ remained between $0.10\,\mathrm{W\,m^{-2}}$ to $0.125\,\mathrm{W\,m^{-2}}$ between August and November 2023. From the 1st January 2023 until 1st November 2024, whilst the mean heating rate anomaly was $-0.09\,\mathrm{K\,d^{-1}}$ at $1\,\mathrm{hPa}$ and $-0.05\,\mathrm{K\,d^{-1}}$ at $0.1\,\mathrm{hPa}$. In Ny-Ålesund, at the start of 2023, there is a notable positive heating rate anomaly in the mesosphere, during a mesospheric dry phase. After April 2023, the effects of the Hunga water vapour injection started to show here, and a negative heating rate anomaly persists in the stratosphere and mesosphere almost without interruption.

Shortwave absorption by water vapour molecules is substantially weaker than their longwave absorption. Nevertheless, to fully assess the total radiative heating rate anomaly, it remains important to include these shortwave contributions alongside
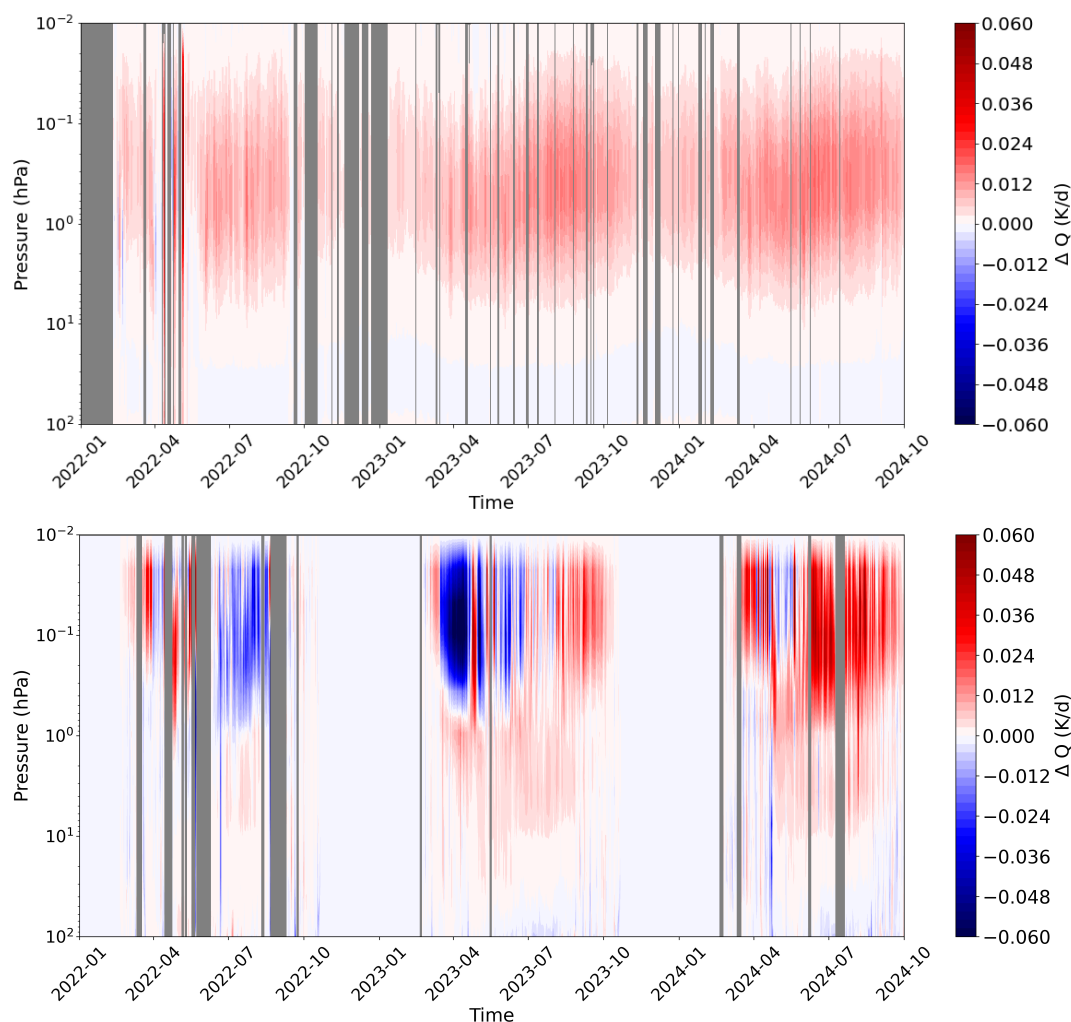
340

15

Figure 8. The heating rate anomaly after the Hunga eruption as a result of the increased short-wave absorption above Zimmerwald (top) and Ny-Ålesund (bottom).

the longwave heating rates. Because water vapour does not significantly emit radiation in the shortwave at middle-atmospheric

345 temperatures, emission was not considered by the radiative transfer model.

From Figure 8, a consistent warming effect of approximately $0.006\,\mathrm{K\,d^{-1}}$ is evident at 1 hPa over Bern. In contrast, a much stronger seasonal cycle is observed in Ny-Ålesund. No heating rates are calculated during the four-month polar night, but around the summer solstice, the relatively large mean daily solar flux at the top of the atmosphere leads to pronounced heating anomalies. Of particular note is the negative heating anomaly in spring 2023 between 0.4 hPa and 0.01 hPa, followed by a

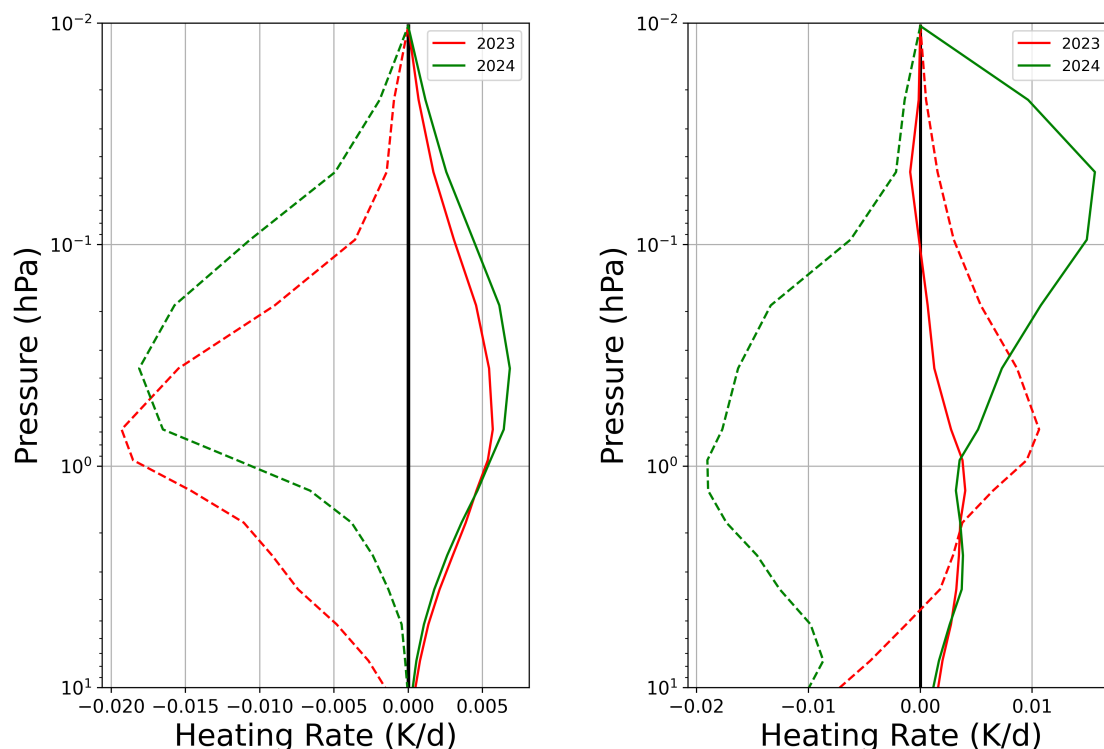350 positive anomaly increasing through summer 2024 at similar pressure levels.

Figure 9. Mean heating rate anomalies for Zimmerwald for the entire year (left) and Ny-Ålesund between mid-February and late October (right), with the anomaly caused through changes in longwave radiances in dashed lines, and shortwave radiances in solid lines.

In Figure 9, the combined effect of longwave and shortwave heating is combined, for whole years above Zimmerwald, and for the outside the polar night (day of year 51 until 287) at Ny-Ålesund. The results show a conclusive net cooling over both years at Zimmerwald, across all altitudes analysed, with a shortwave heating approximately 25% of the longwave cooling impact, with the height of the maximum heating anomaly increasing from 2023 to 2024. In Ny-Ålesund, there is a slightly different picture, with no significant longwave cooling in 2023, and a larger mean impact from shortwave heating that year. In 2024, when there is a more decisive water vapour anomaly, the longwave heating rate is more significant, at $-0.019\,\mathrm{K\,d^{-1}}$ at 1 hPa. However, above 0.15 hPa, the shortwave heating dominates the longwave cooling, and the net impact is positive, with a mean anomaly of $0.01\,\mathrm{K\,d^{-1}}$ for the non-polar night period.

5 Conclusions

Whilst uncertainty persists about how long the anomaly of water vapour in the middle atmosphere will persist, and the global distribution of this increase in water vapour, it is generally agreed that higher than average total middle atmosphere water vapour will persist at least until 2027, with the potential for significant water vapour to remain until 2032 or longer.

The radiative impact studies conducted in this paper have found that the increase in long-wave down-welling fluxes at 10 hPa has outweighed the decrease in short-wave down-welling fluxes by approximately a factor of 10. The climatic impact of this at the surface is admittedly very limited. Whilst the increase in long-wave down-welling flux increased by between $0.010\,\mathrm{W\,m^{-2}}$ to $0.04\,\mathrm{W\,m^{-2}}$ for over $90\,\%$ of the period between March 2023 and May 2025 at Zimmerwald, this is approximately $1\,\%$ of the change due to the increase in carbon dioxide since pre-industrial times ($1.63\,\mathrm{W\,m^{-2}}$ to $2.01\,\mathrm{W\,m^{-2}}$ increase between 1750 and 2011) (Myhre et al., 2013).

A more substantial climatic influence of the Hunga-induced water vapour enhancement may occur through local heating-rate changes within the middle atmosphere. Between 1 January 2023 and 1 January 2025, we find net (long-wave plus short-wave) heating-rate anomalies of about $-0.012\,\mathrm{K\,d^{-1}}$ at $1\,\mathrm{hPa}$ above Zimmerwald and $-0.016\,\mathrm{K\,d^{-1}}$ at $1\,\mathrm{hPa}$ above Ny Alesund, which when sustained over multiple months has the potential to alter middle-atmospheric temperature gradients and winds. Such dynamical shifts can propagate downward, affecting tropospheric circulation and weather patterns. Additionally, these temperature changes could influence stratospheric ozone chemistry, with possible consequences for both climate regulation and surface-level UV radiation.

Data availability. MIAWARA data can be accessed through the landing page at: doi.org/10.60897/pdyc-8v84 and MIAWARA-C can be accessed through the landing page at doi.org/10.60897/gk0h-3b75.

Author contributions. AB ran radiative transfer codes and performed all data analysis with input and suggestions from GS. The manuscript was written by AB, with edits from GS and AM.

Competing interests. Gunter Stober is an editor at Annales Geophysicae.

References

pyarts-fluxes: A Python Wrapper for Simulating Radiative Fluxes with ARTS, https://github.com/atmtools/pyarts-fluxes, accessed: 2024-10-01, 2024.

Basha, G., Ratnam, M. V., Kumar, A. H., Jiang, J. H., Babu, S. R., and Kishore, P.: Impact of Hunga Tonga-Hunga Ha'apai volcanic eruption on stratospheric water vapour, temperature, and ozone, Remote Sensing, 15, 3602, 2023.

Becker, E.: Dynamical Control of the Middle Atmosphere, Space Science Reviews, 168, 283–314, https://doi.org/10.1007/s11214-011-9841-5, 2012.

Bell, A.: Retrieved Water Vapour Profiles from MIAWARA-C at the Ny-Ålesund Observatory, Svalbard, https://doi.org/10.60897/gk0h-3b75, 2025.

Bell, A., Sauvageat, E., Stober, G., Hocke, K., and Murk, A.: Developments on a 22 GHz microwave radiometer and reprocessing of 13-year time series for water vapour studies, Atmospheric Measurement Techniques, 18, 555–567, 2025.

Brath, M., Petersen, J., Buehler, S. A., and Eriksson, P.: Extending the Atmospheric Radiative Transfer Simulator (ARTS) to Shortwave Radiation, Preprint, available at SSRN: https://ssrn.com/abstract=4968132, 2024.

Buehler, S. A., John, V., Kottayil, A., Milz, M., and Eriksson, P.: Efficient radiative transfer simulations for a broadband infrared radiometer—Combining a weighted mean of representative frequencies approach with frequency selection by simulated annealing, Journal of Quantitative Spectroscopy and Radiative Transfer, 111, 602–615, 2010.

Buehler, S. A., Mendrok, J., Eriksson, P., Perrin, A., Larsson, R., and Lemke, O.: ARTS, the atmospheric radiative transfer simulator–version 2.2, Geoscientific Model Development, 11, 1537–1556, 2018.

Carn, S., Krotkov, N., Fisher, B., and Li, C.: Out of the blue: volcanic SO2 emissions during the 2021-2022 Hunga Tonga-Hunga Ha'apai eruptions, Authorea Preprints, 2022.

Carr, J. L., Horváth, A., Wu, D. L., and Friberg, M. D.: Stereo Plume Height and Motion Retrievals for the Record-Setting Hunga Tonga-Hunga Ha'apai Eruption of 15 January 2022, Geophysical Research Letters, 49, e2022GL098131, https://doi.org/https://doi.org/10.1029/2022GL098131, e2022GL098131 2022GL098131, 2022.

Charlesworth, E., Plöger, F., Birner, T., Baikhadzhaev, R., Abalos, M., Abraham, N. L., Akiyoshi, H., Bekki, S., Dennison, F., Jöckel, P., et al.: Stratospheric water vapor affecting atmospheric circulation, Nature Communications, 14, 3925, 2023.

Coddington, O., Lean, J. L., Lindholm, D., Pilewskie, P., Snow, M., and Program, N. C.: NOAA Climate Data Record (CDR) of Solar Spectral Irradiance (SSI), NRLSSI Version 2.1, https://doi.org/10.7289/V53776SW, [ssi_v02r01_monthly_s200401_e200412_c20170717.nc], 2017.

Fernandez, S., Murk, A., and Kämpfer, N.: GROMOS-C, a novel ground-based microwave radiometer for ozone measurement campaigns, atmospheric measurement techniques, 8, 2649–2662, 2015.

Forkman, P., Eriksson, P., and Winnberg, A.: The 22 ghz radio-aeronomy receiver at onsala space observatory, Journal of Quantitative Spectroscopy and Radiative Transfer, 77, 23–42, 2003.

Iacono, M. J., Delamere, J. S., Mlawer, E. J., Shephard, M. W., Clough, S. A., and Collins, W. D.: Radiative forcing by long-lived greenhouse gases: Calculations with the AER radiative transfer models, Journal of Geophysical Research: Atmospheres, 113, 2008.

Jenkins, S., Smith, C., Allen, M., and Grainger, R.: Tonga eruption increases chance of temporary surface temperature anomaly above 1.5° C, Nature Climate Change, 13, 127–129, 2023.

Jucker, M., Lucas, C., and Dutta, D.: Long-term surface impact of Hunga Tonga-Hunga Ha'apai-like stratospheric water vapor injection, Authorea Preprints, 2023.

Kirkpatrick, S., Gelatt Jr, C. D., and Vecchi, M. P.: Optimization by simulated annealing, science, 220, 671–680, 1983.

425 Krochin, W., Navas-Guzmán, F., Kuhl, D., Murk, A., and Stober, G.: Continuous temperature soundings at the stratosphere and lower mesosphere with a ground-based radiometer considering the Zeeman effect, Atmospheric Measurement Techniques, 15, 2231–2249, https://doi.org/10.5194/amt-15-2231-2022, 2022.

Lindzen, R. S.: Turbulence and stress owing to gravity wave and tidal breakdown, Journal of Geophysical Research: Oceans, 86, 9707–9714, https://doi.org/10.1029/JC086iC10p09707, 1981.

430 Matoza, R. S., Fee, D., Assink, J. D., Iezzi, A. M., Green, D. N., Kim, K., Toney, L., Lecocq, T., Krishnamoorthy, S., Lalande, J.-M., Nishida, K., Gee, K. L., Haney, M. M., Ortiz, H. D., Brissaud, Q., Martire, L., Rolland, L., Vergados, P., Nippress, A., Park, J., Shani-Kadmiel, S., Witsil, A., Arrowsmith, S., Caudron, C., Watada, S., Perttu, A. B., Taisne, B., Mialle, P., Pichon, A. L., Vergoz, J., Hupe, P., Blom, P. S., Waxler, R., Angelis, S. D., Snively, J. B., Ringler, A. T., Anthony, R. E., Jolly, A. D., Kilgour, G., Averbuch, G., Ripepe, M., Ichihara, M., Arciniega-Ceballos, A., Astafyeva, E., Ceranna, L., Cevuard, S., Che, I.-Y., Negri, R. D., Ebeling, C. W., Evers, L. G., Franco-Marin, L. E.,

435 Gabrielson, T. B., Hafner, K., Harrison, R. G., Komjathy, A., Lacanna, G., Lyons, J., Macpherson, K. A., Marchetti, E., McKee, K. F., Mellors, R. J., Mendo-Pérez, G., Mikesell, T. D., Munaibari, E., Oyola-Merced, M., Park, I., Pilger, C., Ramos, C., Ruiz, M. C., Sabatini, R., Schwaiger, H. F., Tailpied, D., Talmadge, C., Vidot, J., Webster, J., and Wilson, D. C.: Atmospheric waves and global seismoacoustic observations of the January 2022 Hunga eruption, Tonga, Science, 377, 95–100, https://doi.org/10.1126/science.abo7063, 2022.

Millan, L., Santee, M. L., Lambert, A., Livesey, N. J., Werner, F., Schwartz, M. J., Pumphrey, H. C., Manney, G. L., Wang, Y., Su, H., et al.:

440 The Hunga Tonga-Hunga Ha'apai hydration of the stratosphere, Geophysical Research Letters, 49, e2022GL099 381, 2022.

Myhre, G., Shindell, D., Bréon, F. M., Collins, W., Fuglestvedt, J., Huang, J., Koch, D., Lamarque, J. F., Mendoza, B., Nakajima, T., Robock, A., Stephens, G., Takemura, T., and Zhang, H.: Anthropogenic and Natural Radiative Forcing, in: Climate Change 2013: The Physical Science Basis. Contribution of Working Group I to the Fifth Assessment Report of the Intergovernmental Panel on Climate Change, edited by Stocker, T. F., Qin, D., Plattner, G. K., Tignor, M., Allen, S. K., Boschung, J., Nauels, A., Xia, Y., Bex, V., and Midgley, P. M., pp.

445 659–740, Cambridge University Press, Cambridge, United Kingdom and New York, NY, USA, https://www.ipcc.ch/site/assets/uploads/2018/02/WG1AR5_Chapter08_FINAL.pdf, 2013.

NASA JPL: Microwave Limb Sounder (MLS) Mission Overview, https://mls.jpl.nasa.gov/, accessed: 2024-07-24, 2024.

Nedoluha, G. E., Gomez, R. M., Boyd, I., Neal, H., Allen, D. R., Lambert, A., and Livesey, N. J.: Measurements of Stratospheric Water Vapor at Mauna Loa and the Effect of the Hunga Tonga Eruption, Journal of Geophysical Research: Atmospheres, 128, e2022JD038 100,

450 2023.

Nedoluha, G. E., Gomez, R. M., Boyd, I., Neal, H., Allen, D. R., and Lambert, A.: The spread of the Hunga Tonga H2O plume in the middle atmosphere over the first two years since eruption, Journal of Geophysical Research: Atmospheres, 129, e2024JD040 907, 2024.

Rhodes, B.: PyEphem: Astronomical computations for Python, https://github.com/brandon-rhodes/pyephem, giTHub repository, 2023.

Sauvageat, E., Maillard Barras, E., Hocke, K., Haefele, A., and Murk, A.: Harmonized retrieval of middle atmospheric ozone from two

455 microwave radiometers in Switzerland, Atmospheric Measurement Techniques, 15, 6395–6417, 2022.

Schoeberl, M., Wang, Y., Ueyama, R., Taha, G., and Yu, W.: The cross equatorial transport of the Hunga Tonga-Hunga Ha'apai eruption plume, Geophysical Research Letters, 50, e2022GL102 443, 2023a.

Schoeberl, M. R., Wang, Y., Ueyama, R., Taha, G., Jensen, E., and Yu, W.: Analysis and impact of the Hunga Tonga-Hunga Ha'apai stratospheric water vapor plume, Geophysical Research Letters, 49, e2022GL100 248, 2022.

460   Schoeberl, M. R., Wang, Y., Ueyama, R., Dessler, A., Taha, G., and Yu, W.: The Estimated Climate Impact of the Hunga Tonga-Hunga
          Ha'apai Eruption Plume, Geophysical Research Letters, 50, e2023GL104 634, 2023b.

      Schranz, F., Fernandez, S., Kämpfer, N., and Palm, M.: Diurnal variation in middle-atmospheric ozone observed by ground-based microwave
          radiometry at Ny-Ålesund over 1 year, Atmospheric Chemistry and Physics, 18, 4113–4130, https://doi.org/10.5194/acp-18-4113-2018,
          2018.

465   Schranz, F., Tschanz, B., Rüfenacht, R., Hocke, K., Palm, M., and Kämpfer, N.: Investigation of Arctic middle-atmospheric dynamics using
          3 years of H_2O and O_3 measurements from microwave radiometers at Ny-Ålesund, Atmospheric Chemistry and Physics, 19, 9927–9947,
          https://doi.org/10.5194/acp-19-9927-2019, 2019.

      Schranz, F., Hagen, J., Stober, G., Hocke, K., Murk, A., and Kämpfer, N.: Small-scale variability of stratospheric ozone during the sud-
          den stratospheric warming 2018/2019 observed at Ny-Ålesund, Svalbard, Atmospheric Chemistry and Physics, 20, 10 791–10 806,
470   https://doi.org/10.5194/acp-20-10791-2020, 2020.

      Schwartz, M. J., Lambert, A., Manney, G. L., Read, W. G., Livesey, N. J., Froidevaux, L., Ao, C. O., Bernath, P. F., Boone, C. D., Cofield,
          R. E., Daffer, W. H., Drouin, B. J., Fetzer, E. J., Fuller, R. A., Jarnot, R. F., Jiang, J. H., Jiang, Y. B., Knosp, B. W., Krüger, K., Li, J.-L. F.,
          Mlynczak, M. G., Pawson, S., Russell III, J. M., Santee, M. L., Snyder, W. V., Stek, P. C., Thurstans, R. P., Tompkins, A. M., Wagner,
          P. A., Walker, K. A., Waters, J. W., and Wu, D. L.: Validation of the Aura Microwave Limb Sounder temperature and geopotential height
475   measurements, Journal of Geophysical Research: Atmospheres, 113, https://doi.org/https://doi.org/10.1029/2007JD008783, 2008.

      SciPy Community: scipy.interpolate.interp1d, https://docs.scipy.org/doc/scipy/reference/generated/scipy.interpolate.interp1d.html, accessed:
          2024-08-15, 2024.

      Sellitto, P., Podglajen, A., Belhadji, R., Boichu, M., Carboni, E., Cuesta, J., Duchamp, C., Kloss, C., Siddans, R., Bègue, N., et al.: The
          unexpected radiative impact of the Hunga Tonga eruption of 15th January 2022, Communications Earth & Environment, 3, 288, 2022.

480   Sheese, P. E., Walker, K. A., Boone, C. D., Bernath, P. F., Froidevaux, L., Funke, B., Raspollini, P., and von Clarmann, T.: ACE-FTS
          ozone, water vapour, nitrous oxide, nitric acid, and carbon monoxide profile comparisons with MIPAS and MLS, Journal of Quantitative
          Spectroscopy and Radiative Transfer, 186, 63–80, 2017.

      Shi, G., Krochin, W., Sauvageat, E., and Stober, G.: Ozone and water vapor variability in the polar middle atmosphere observed with ground-
          based microwave radiometers, Atmospheric Chemistry and Physics, 23, 9137–9159, https://doi.org/10.5194/acp-23-9137-2023, 2023.

485   Shi, G., Krochin, W., Sauvageat, E., and Stober, G.: Ozone anomalies over the polar regions during stratospheric warming events, Atmo-
          spheric Chemistry and Physics, 24, 10 187–10 207, https://doi.org/10.5194/acp-24-10187-2024, 2024.

      Sicard, M., Baron, A., Ranaivombola, M., Gantois, D., Millet, T., Sellitto, P., Bègue, N., Bencherif, H., Payen, G., Marquestaut, N., et al.:
          Radiative impact of the Hunga stratospheric volcanic plume: role of aerosols and water vapor over Réunion Island (21° S, 55° E), Atmo-
          spheric Chemistry and Physics, 25, 367–381, 2025.

490   Smith, A. K.: Global Dynamics of the MLT, Surveys in Geophysics, 33, 1177–1230, https://doi.org/10.1007/s10712-012-9196-9, 2012.

      Solomon, S., Rosenlof, K. H., Portmann, R. W., Daniel, J. S., Davis, S. M., Sanford, T. J., and Plattner, G.-K.: Contributions of stratospheric
          water vapor to decadal changes in the rate of global warming, Science, 327, 1219–1223, 2010.

      Stober, G., Liu, A., Kozlovsky, A., Qiao, Z., Krochin, W., Shi, G., Kero, J., Tsutsumi, M., Gulbrandsen, N., Nozawa, S., Lester, M., Baum-
          garten, K., Belova, E., and Mitchell, N.: Identifying gravity waves launched by the Hunga Tonga–Hunga Ha'apai volcanic eruption in
495   mesosphere/lower-thermosphere winds derived from CONDOR and the Nordic Meteor Radar Cluster, Annales Geophysicae, 41, 197–
          208, https://doi.org/10.5194/angeo-41-197-2023, 2023.

Stober, G., Vadas, S. L., Becker, E., Liu, A., Kozlovsky, A., Janches, D., Qiao, Z., Krochin, W., Shi, G., Yi, W., Zeng, J., Brown, P., Vida, D., Hindley, N., Jacobi, C., Murphy, D., Buriti, R., Andrioli, V., Batista, P., Marino, J., Palo, S., Thorsen, D., Tsutsumi, M., Gulbrandsen, N., Nozawa, S., Lester, M., Baumgarten, K., Kero, J., Belova, E., Mitchell, N., Moffat-Griffin, T., and Li, N.: Gravity waves generated by the Hunga Tonga–Hunga Ha'apai volcanic eruption and their global propagation in the mesosphere/lower thermosphere observed by meteor radars and modeled with the High-Altitude general Mechanistic Circulation Model, Atmospheric Chemistry and Physics, 24, 4851–4873, https://doi.org/10.5194/acp-24-4851-2024, 2024.

Terry, J. P., Goff, J., Winspear, N., Bongolan, V. P., and Fisher, S.: Tonga volcanic eruption and tsunami, January 2022: Globally the most significant opportunity to observe an explosive and tsunamigenic submarine eruption since AD 1883 Krakatau, Geoscience Letters, 9, 24, 2022.

Themens, D. R., Watson, C., Žagar, N., Vasylkevych, S., Elvidge, S., McCaffrey, A., Prikryl, P., Reid, B., Wood, A., and Jayachandran, P. T.: Global propagation of ionospheric disturbances associated with the 2022 Tonga volcanic eruption, Geophysical Research Letters, 49, e2022GL098 158, https://doi.org/10.1029/2022GL098158, 2022.

Tschanz, B., Straub, C., Scheiben, D., Walker, K., Stiller, G., and Kämpfer, N.: Validation of middle atmospheric campaign-based water vapour measured by the ground-based microwave radiometer MIAWARA-C, Atmospheric Measurement Techniques Discussions, 6, 1311–1359, 2013.

Vadas, S. L., Becker, E., Figueiredo, C., Bossert, K., Harding, B. J., and Gasque, L. C.: Primary and Secondary Gravity Waves and Large-Scale Wind Changes Generated by the Tonga Volcanic Eruption on 15 January 2022: Modeling and Comparison With ICON-MIGHTI Winds, Journal of Geophysical Research: Space Physics, 128, e2022JA031 138, https://doi.org/10.1029/2022JA031138, 2023a.

Vadas, S. L., Figueiredo, C., Becker, E., Huba, J. D., Themens, D. R., Hindley, N. P., Mrak, S., Galkin, I., and Bossert, K.: Traveling ionospheric disturbances induced by the secondary gravity waves from the Tonga eruption on 15 January 2022: Modeling with MESO-RAC/HIAMCM/SAMI3 and comparison with GPS/TEC and ionosonde data, Journal of Geophysical Research: Space Physics, n/a, e2023JA031 408, https://doi.org/10.1029/2023JA031408, 2023b.

Waters, J. W., Froidevaux, L., Harwood, R. S., Jarnot, R. F., Pickett, H. M., Read, W. G., Siegel, P. H., Cofield, R. E., Filipiak, M. J., Flower, D. A., et al.: The earth observing system microwave limb sounder (EOS MLS) on the Aura satellite, IEEE transactions on geoscience and remote sensing, 44, 1075–1092, 2006.

Wright, C. J., Hindley, N. P., Alexander, M. J., Barlow, M., Hoffmann, L., Mitchell, C. N., Prata, F., Bouillon, M.and Carstens, J., Clerbaux, C., Osprey, S. M., Powell, N., Randall, C. E., and Yue, J.: Surface-to-space atmospheric waves from Hunga Tonga-Hunga Ha'apai eruption, Nature, 609, 741–746, https://doi.org/https://doi.org/10.1038/s41586-022-05012-5, 2022.

Yu, W., Garcia, R., Yue, J., Smith, A., Wang, X., Randel, W., Qiao, Z., Zhu, Y., Harvey, V. L., Tilmes, S., et al.: Mesospheric temperature and circulation response to the Hunga Tonga-Hunga-Ha'apai volcanic eruption, Journal of Geophysical Research: Atmospheres, 128, e2023JD039 636, 2023.